Supplementary information

Interface-engineered melt-spun BiSbTe for multiscale phonon scattering and enhanced thermoelectric performance

Yae Eun Park,[a†] Hyunjin Han,[a†] Sung-Jin Jung,[b†] Junwoo Song,[b] Jino Kim,[b] Jungwon Na,[b] Kwangjoo Kim,[b] Insub Lee,[b] Hoon Wee,[b] Joonhyun Lee,[b] Sungjun Yang,[c] Seungki Jo,[d] Ho Seong Lee,[e] Tae Joo shin,[f] Youngdeog Koh,*[b] and Jae Sung Son*[a]

[a]*Department of Chemical Engineering, Pohang University of Science and Technology, Pohang, Republic of Korea.*

[b]*Samsung Research, Samsung Electronics, Seoul, Republic of Korea.*

[c] *Office of Research Facilities and Training (ResFacT), Ulsan National Institute of Science and Technology (UNIST), Ulsan, Republic of Korea*

[d] *Nano materials Research Division, Korea Institute of Materials Science (KIMS), Changwon, Republic of Korea.*

[e] *Department of Materials Science and Metallurgical Engineering, Kyungpook National University, Daegu, Republic of Korea.*

[f] *School of Semiconductor Materials and Devices Engineering, Ulsan National Institute of Science and Technology (UNIST), Ulsan, Republic of Korea.*

* Correspondence: yd.koh@samsung.com, sonjs@postech.ac.kr

1. Experimental Section

1.1 Materials

Ammonium phosphomolybdate hydrate was purchased from Sigma-Aldrich. Ethyl alcohol (99.5%) was purchased from SAMCHUN PURE CHEMICAL CO., LTD. All chemicals were used without further purification.

1.2 Synthesis of POM-coated BiSbTe

The p-type $Bi_{0.5}Sb_{1.5}Te_3$ powders were synthesized via the melt-spinning process, ensuring a controlled stoichiometric composition. Following melt spinning, the ribbons were pulverized into fine powders. A solution was prepared by dispersing 0.1–0.5 mol% of POM in 5 mL of ethanol. Subsequently, 3 g of the Bi–Sb–Te powder was added to this solution and stirred at 1200 rpm for 10 hours. After stirring, the mixture was dried under vacuum to obtain the coated powder. These powders were then sintered by spark plasma sintering (SPS) under a pressure of 45 MPa at 450 °C.

1.3 Material Characterization

X-ray diffraction (XRD) patterns were collected before sintering using a D/MAX-2500V (Rigaku) operated at 40 kV and 200 mA, and after sintering using a D6 PHASER (Bruker) operated at 20 kV and 5 mA, both employing Cu Kα radiation (λ = 0.154 nm) over a 2θ range of 10–70°. The microstructure analysis was examined by scanning electron microscopy (SEM, Hitachi S-3400N) at an operating voltage of 10 kV. The particle size distribution of the stirred melt-spun powders without POM was measured by laser diffraction using Mastersizer 3000+ (Malvern Panalytical). Electron backscatter diffraction (EBSD) and energy dispersive spectroscopy (EDS) mapping were performed by scanning electron microscopy (SEM, Hitachi) equipped with Velocity Ultra at operating voltage of 15 kV. Electron energy-loss spectroscopy (EELS) was performed using high-resolution field-emission transmission electron microscopy (HR FE-TEM, JEM-2200FS with Image Cs-corrector) and the microstructures analysis of the samples were examined using HR FE-TEM (JEOL JEM-2100F with Cs Corrector on STEM). The thermogravimetric analysis (TGA, TA Instruments SDT-Q600) was carried out under air atmosphere, ranging from room temperature to 600 ℃ at a heating rate of 2 ℃/min. The carrier concentrations and mobility were evaluated using equipment of HCS-1, LINSEIS, capable of generating dual opposing magnetic fields of ±0.7 T. The electrical conductivity and Seebeck coefficient were measured simultaneously using a LSR (Linseis, LSR-3) system over the temperature range of 298–523 K. The thermal diffusivity (α) was measured by laser flash

analysis (Linseis, LFA 500), and the total thermal conductivity (κ) was calculated from the relation $\kappa = \rho C_p D$, where ρ is the density, C_p is the specific heat capacity and D is the thermal diffusivity. The specific heat capacity was calculated using the Dulong–Petit equation.

Model of lattice thermal conductivity

In this study, we developed a systematic thermal model to understand the reduction in lattice thermal conductivity. The Debye–Callaway model describes the total phonon relaxation time (τ_tot) as the reciprocal sum of individual relaxation times, assuming that acoustic phonons dominate the lattice thermal conductivity.[C1,2] The lattice thermal conductivity is expressed as

$$\kappa_{lat} = \frac{k_B}{2\pi^2 v}\left(\frac{k_B T}{\hbar}\right)\int_0^{\theta_a/T} \tau_{tot}(x)\frac{x^4 e^x}{(e^x-1)^2}dx \quad (1)$$

where $k_B$is the Boltzmann constant, $\hbar$ is the reduced Plank constant, x is $\hbar\omega/k_B T$ with a phonon angular frequency of ω, v is the average sound speed, θ_a is the Debye temperature, and τ_{tot} is the total phonon relaxation time. According to Matthiessen's rule, the total phonon relaxation time (τ_{tot}) can be expressed as the reciprocal sum of individual scattering processes:

$${\tau_{tot}}^{-1} = {\tau_U}^{-1} + {\tau_N}^{-1} + {\tau_{PD}}^{-1} + {\tau_B}^{-1} + {\tau_{DC}}^{-1} + {\tau_{DS}}^{-1} + {\tau_P}^{-1} \quad (2)$$

In this model, we considered Umklapp phonon–phonon scattering, normal phonon–phonon scattering, point-defect scattering, grain boundary scattering, dislocation scattering, and nano-precipitate scattering.

To further analyze the scattering mechanisms, the spectral lattice thermal conductivity was also calculated as

$$\kappa_s = C_v(\omega)\cdot v^2(\omega)\cdot \tau(\omega) \quad (3)$$

The Umklapp phonon-phonon scattering (τ_U) is calculated from equation (4):

$${\tau_U}^{-1} = A_N \frac{2}{(6\pi^2)^{1/3}}\frac{k_B V^{1/3}\gamma^2\omega^2 T}{M v^3} \quad (4)$$

where V is the atomic volume of matrix, γ is the Grüneisen parameter, T is the absolute temperature, and M is the atomic mass of sample, respectively. A_N is an additional parameter of normal phonon-phonon scattering time and 2.6 is used from the literature data.[C3]

Point-defect scattering originates from atomic size disorder in alloy systems and is described by equation (5):

$${\tau_{PD}}^{-1} = \frac{V\omega^4}{4\pi v^3}\Gamma \quad (5)$$

$$\Gamma = x(x-1)\left[\left(\frac{\Delta M}{M}\right)^2 + \frac{2}{9}\left\{(G+6.4\gamma)\frac{1+r}{1-r}\right\}^2\left(\frac{\Delta a}{a}\right)^2\right] \quad (6)$$

where x, ΔM , G, r, and Δa are the fractional concentration of constituents, difference in mass, a fractional ratio of bulk modulus, Poisson ratio, and the difference in lattice constant, respectively.

The relaxation time by grain boundary scattering is given by equation (7):

$$\tau_B^{-1} = \frac{v}{d} \qquad (7)$$

where the d is the average grain size.

The TEM images in Fig. 3 reveal the formation of dislocations induced by rapid solidification during the melt-spinning process. Therefore, we considered a weak contribution of dislocations within the range of approximately 10^{10} cm^{-2}.[C3]

Dislocation core is shown in equation (8):

$$\tau_{DC}^{-1} = N_D \frac{V^{4/3}}{v^2} \omega^3 \qquad (8)$$

And dislocation strain is shown in equation (9):

$$\tau_{DS}^{-1} = 0.6 \times B_D^2 N_D (\gamma + \gamma_1)^2 \left[\frac{1}{2} + \frac{1}{24}\left(\frac{1-2r}{1-r}\right)^2 \left\{1 + \sqrt{2}\left(\frac{v_L}{v_T}\right)^2\right\}^2\right] \omega \qquad (9)$$

where N_D, B_D, γ_1, v_L, and v_T are the dislocation density, magnitude of Burgers vector, Change in Grüneisen parameter, Longitudinal phonon velocity along a-plane, and Transverse phonon velocity along a-plane, respectively.

$$\gamma_1 = \frac{V_{Sb_2Te_3} C_0 K}{k_B T_a} (\gamma \alpha^2 - \alpha\beta) \qquad (10)$$

$$\alpha = \frac{(V_{Bi_2Te_3} - V_{Sb_2Te_3})}{V_{Sb_2Te_3}} \qquad (11)$$

$$\beta = \frac{(M_{Sb_2Te_3} - M_{Bi_2Te_3})}{2M_{Sb_2Te_3}} \qquad (12)$$

where $V_{Sb_2Te_3}$, $V_{Bi_2Te_3}$, C_0, K, T_a, $M_{Sb_2Te_3}$, $M_{Bi_2Te_3}$ are the atomic volume of Sb_2Te_3, Bi_2Te_3, concentration of Bi_2Te_3 in $Bi_{0.5}Sb_{1.5}Te_3$, bulk modulus of Sb_2Te_3, annealing temperature, average atomic mass of Sb_2Te_3 and Bi_2Te_3, respectively.

In this study, we considered additional phonon scattering by nanometer-scale secondary phases consisting of Mo-rich oxide precipitate. The TEM image shows abundant nano Mo-rich oxide with average diameter of the ~100 nm. Thus, it is reasonable to consider the phonon scattering by interfaces and distance between the nano-precipitates.[C4-6] Assuming nano-precipitates have same diameter in matrix material, we perform the calculation using the Matthiessen-type interpolation between the short- and long-wavelength scattering regimes.[C7-9]

The relaxation time can be shown as:

$$\tau_P{}^{-1} = \upsilon(\sigma_s^{-1} + \sigma_l^{-1}) V_p \qquad (13)$$

where $\sigma_s = 2\pi R^2$, $\sigma_l = \frac{4}{9}\pi R^2 \left(\frac{\Delta D}{D}\right)^2 \left(\frac{R}{\upsilon}\omega\right)^4$; R is the average radius of nano-precipitate, D is the density of matrix, ΔD is the difference of density between the nano-precipitate and matrix, and

V_p is the density of the nano-precipitate. Using the equation, we fitted the average distance. All parameters are represented in the table.

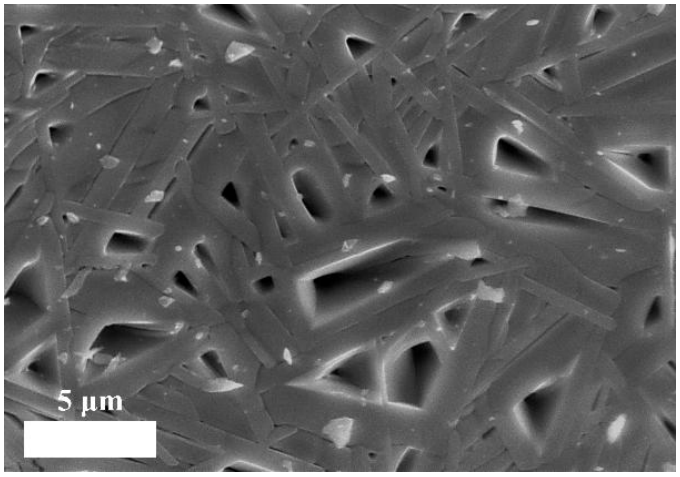

Fig. S1 SEM images of melt-spun BiSbTe powders.

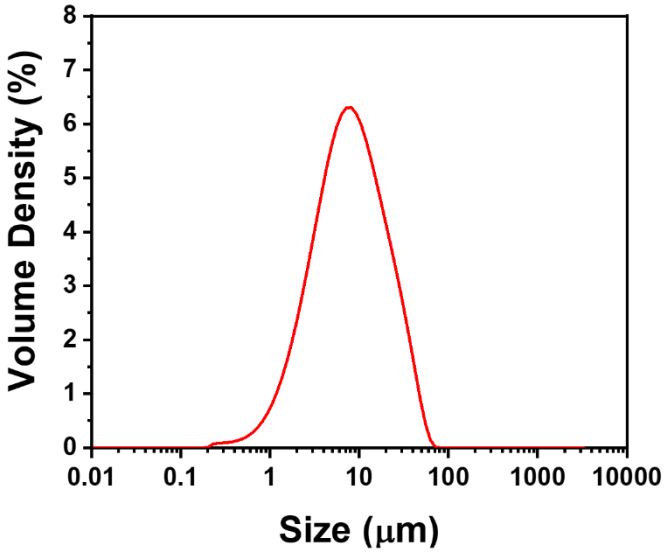

Fig. S2 Particle size distribution of the sample obtained from laser diffraction analysis.

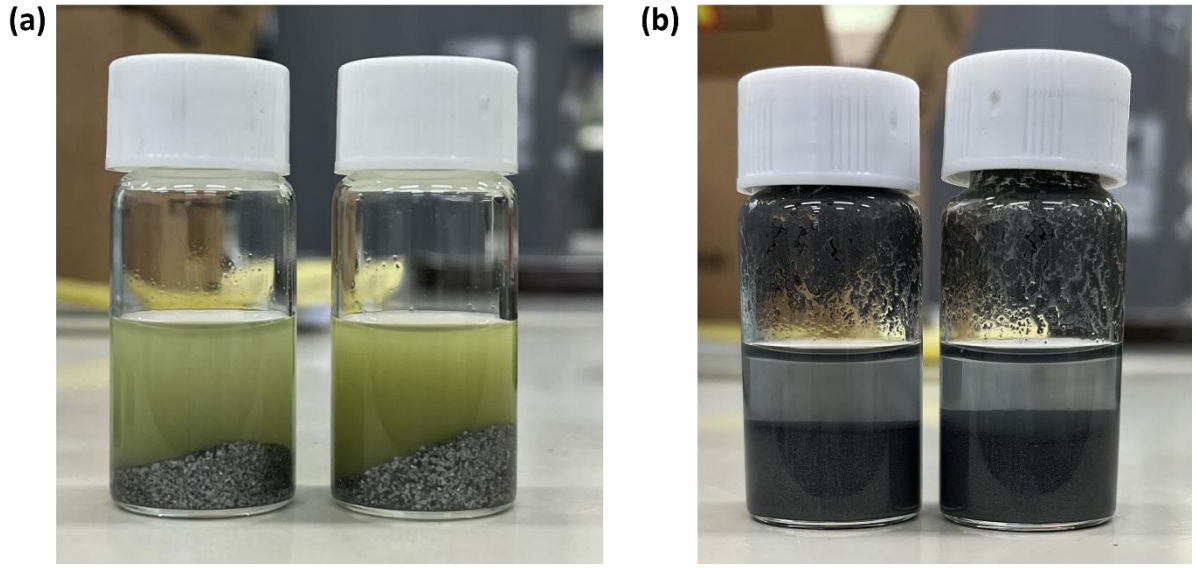

Fig. S3 Photographic images of thermoelectric (TE) powders in EtOH solvent (a) before coating and (b) after coating.

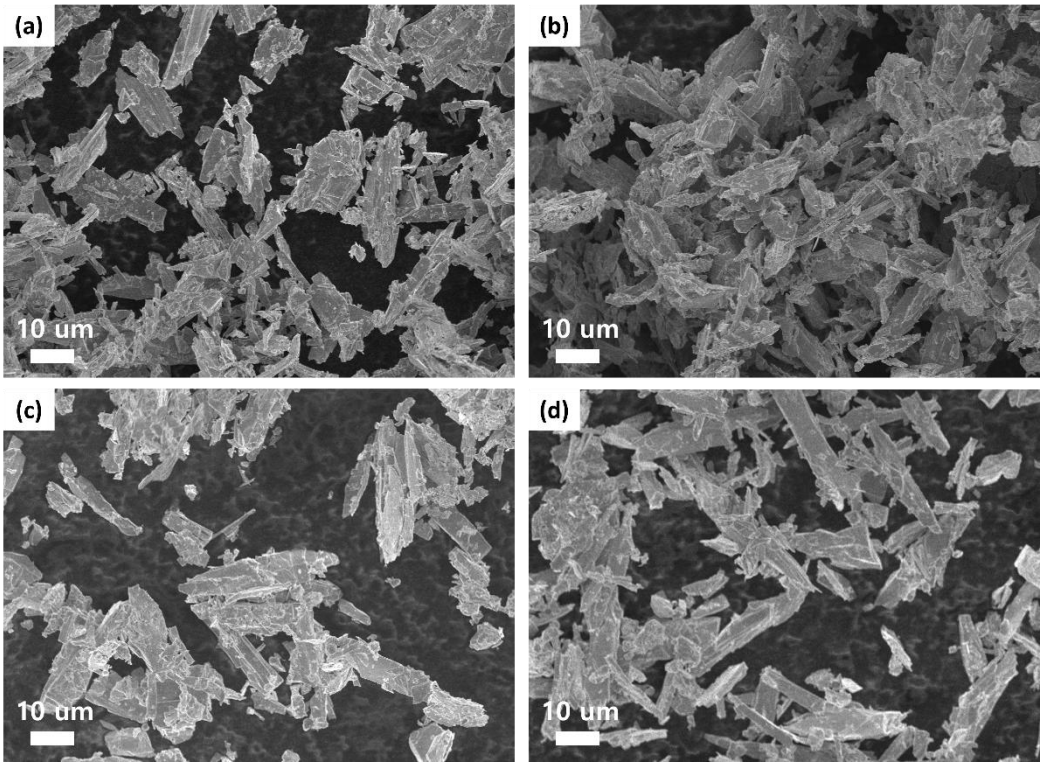

Fig. S4 SEM images of the BiSbTe powder with (a) 0 mol%, (b) 0.1 mol%, (c) 0.3 mol% and (d) 0.5 mol% POM content before sintering.

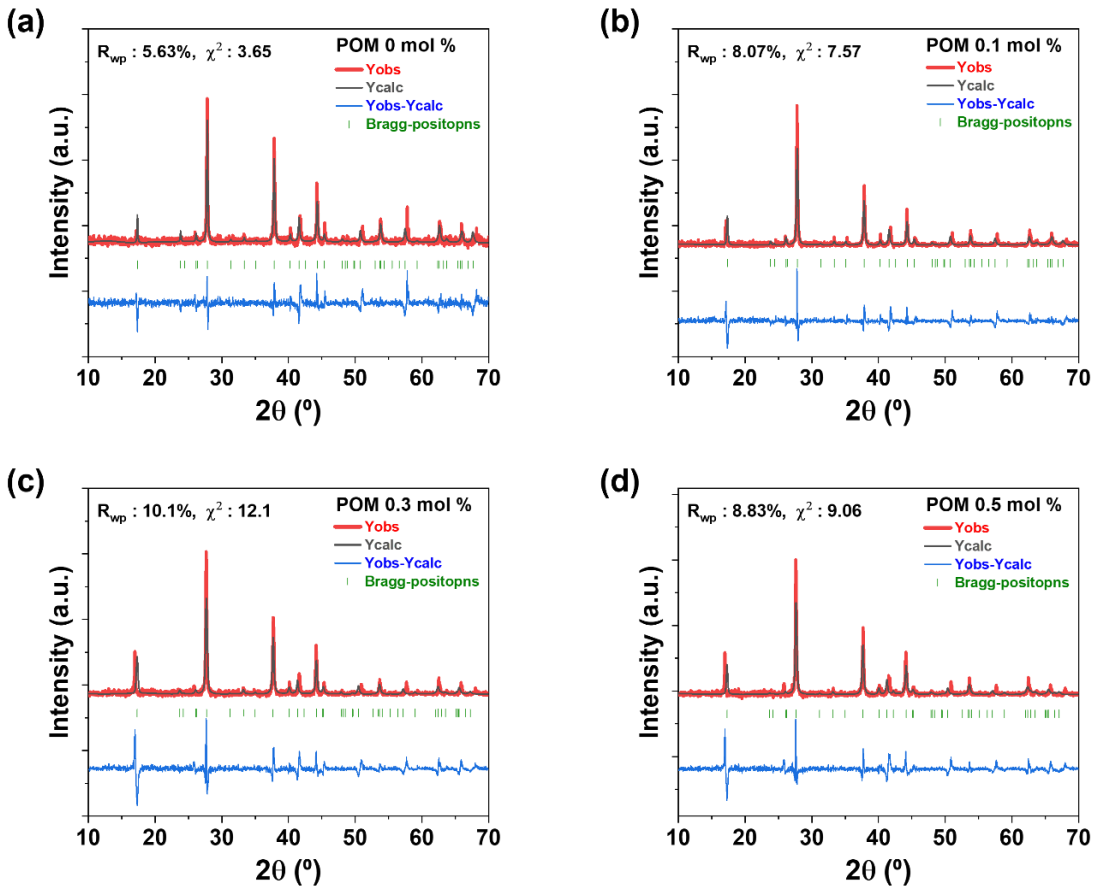

Fig. S5 Full pattern matching refinement (using Le Bail method) of X-ray diffraction patterns for (a) 0 mol%, (b) 0.1 mol%, (c) 0.3 mol% and (d) 0.5 mol% POM. Observed (red line), calculated (black line), and difference (blue line) plots obtained for the full pattern matching refinement of X-ray diffraction data.

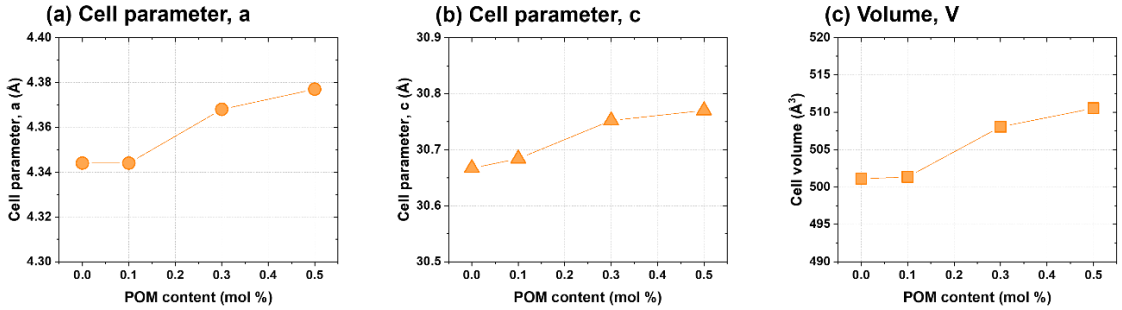

Fig. S6 Evolution of the Le Bail refined lattice parameters (a) *a*, (b) *c* and (c) cell volume as a function of POM content (mol%).

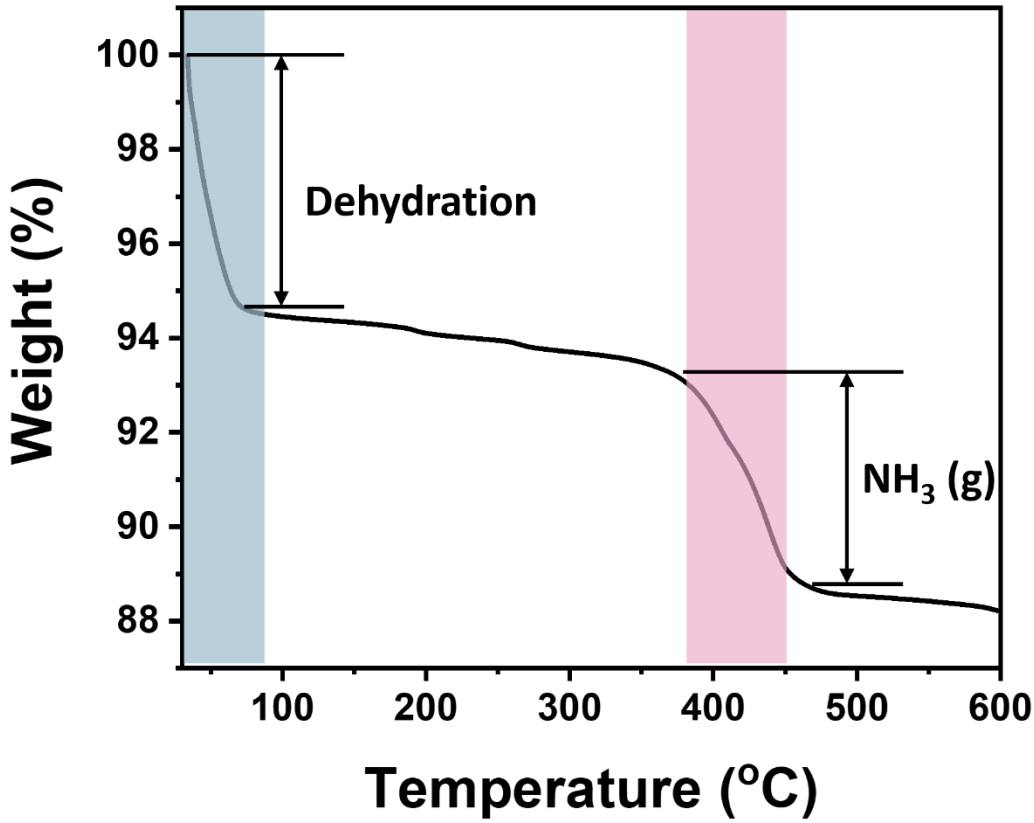

Fig. S7 Thermogravimetric analysis (TGA) of POM.

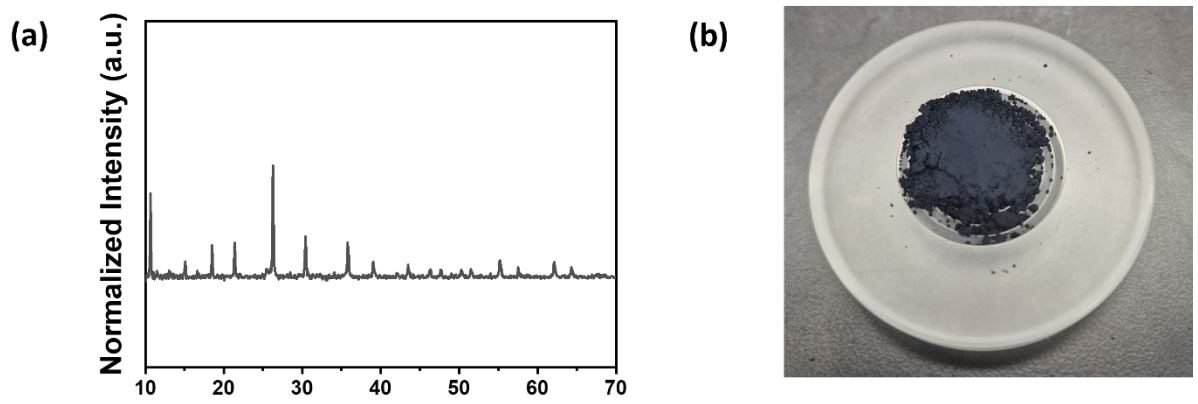

Fig. S8 (a) XRD pattern and (b) photographic image of heat-treated POM at 450 ºC.

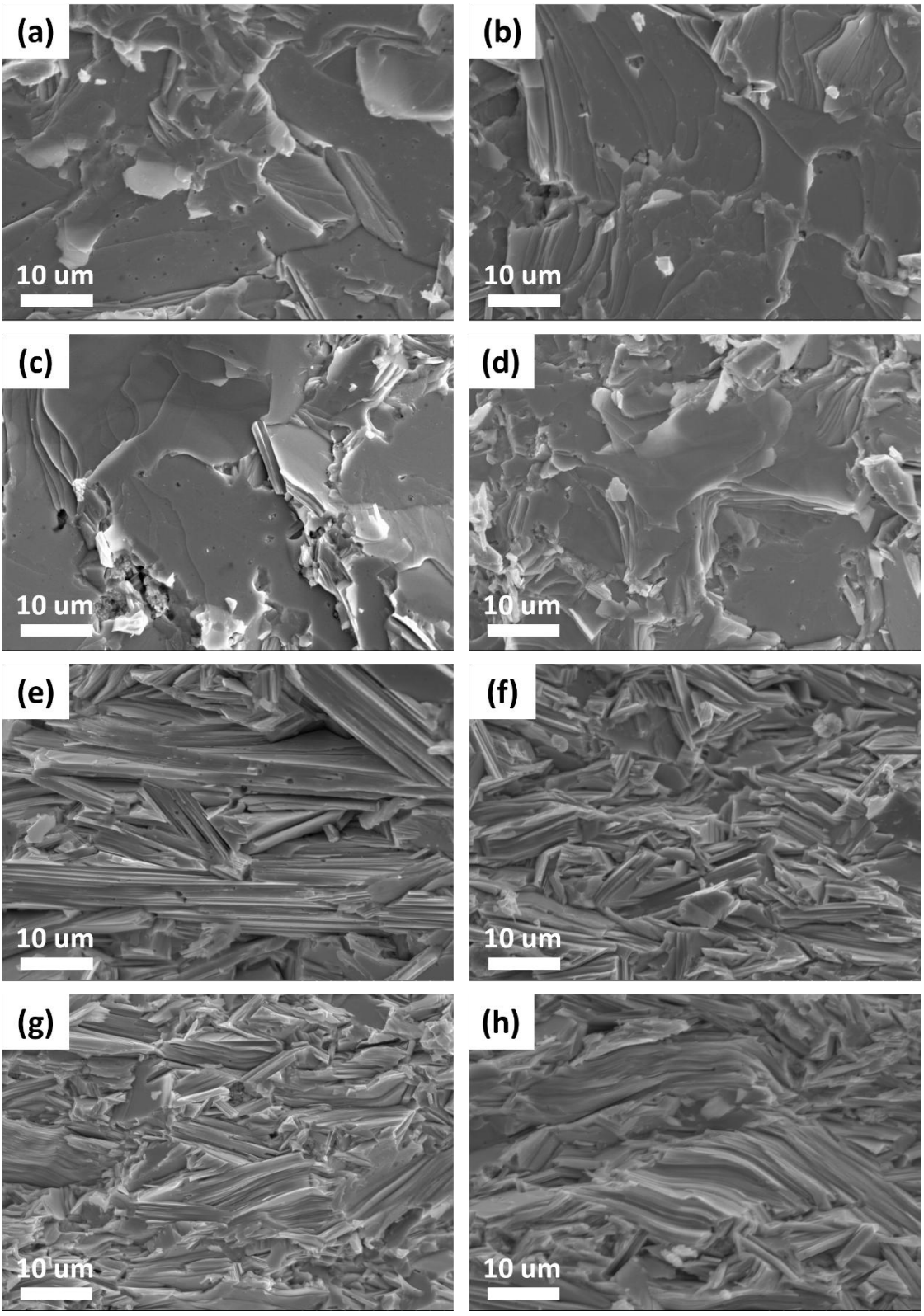

Fig. S9 SEM images of fractured in-plane surface of (a) 0 mol%, (b) 0.1 mol%, (c) 0.3 mol%, and (d) 0.5 mol% POM-coated BiSbTe. SEM images of fractured through-plane surface of (e) 0 mol%, (f) 0.1 mol%, (g) 0.3 mol%, and (h) 0.5 mol% POM-coated BiSbTe.

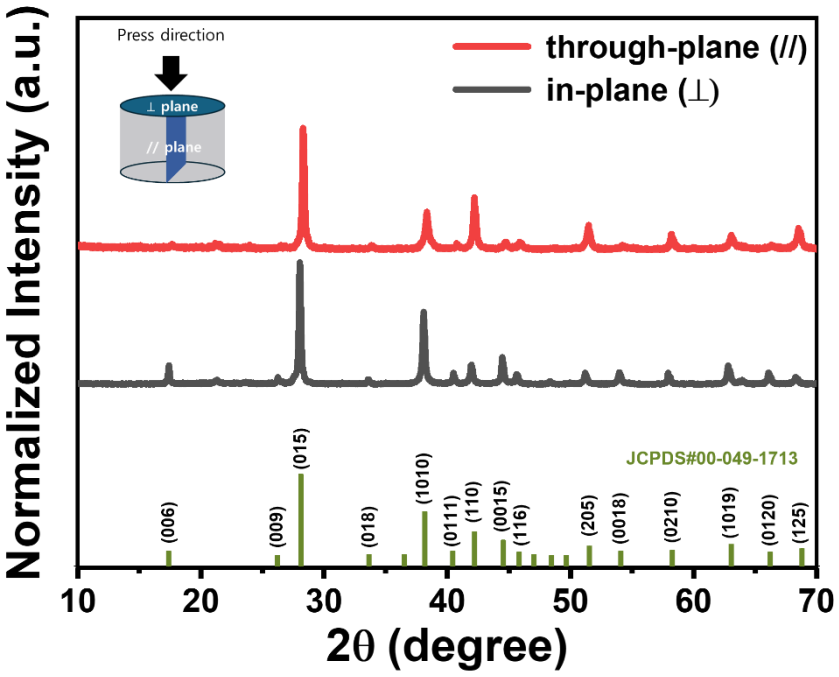

Fig. S10 XRD patterns of SPS-ed 0.1 mol% POM-coated BiSbTe in through-plane (red) and in-plane (black) direction.

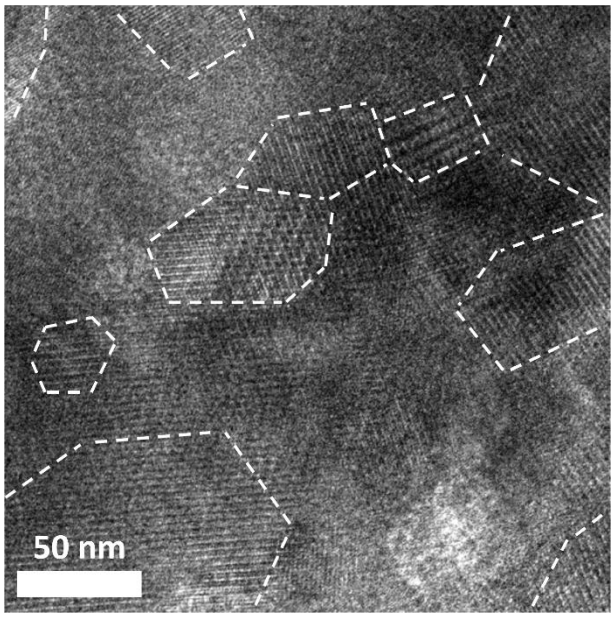

Fig. S11 HRTEM images showing nanocrystal domains in melt-spun and SPS-ed BiSbTe without POM.

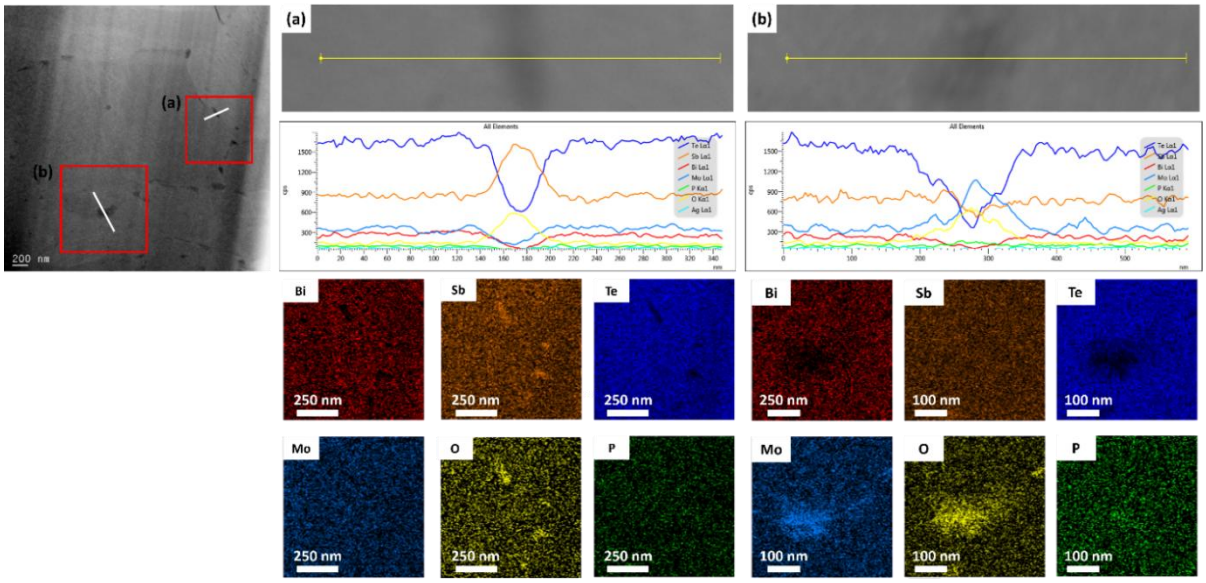

Fig. S12 EDS line scanning profile and mapping image of (a) Sb-rich oxide precipitates and (b) Mo-rich oxide precipitates.

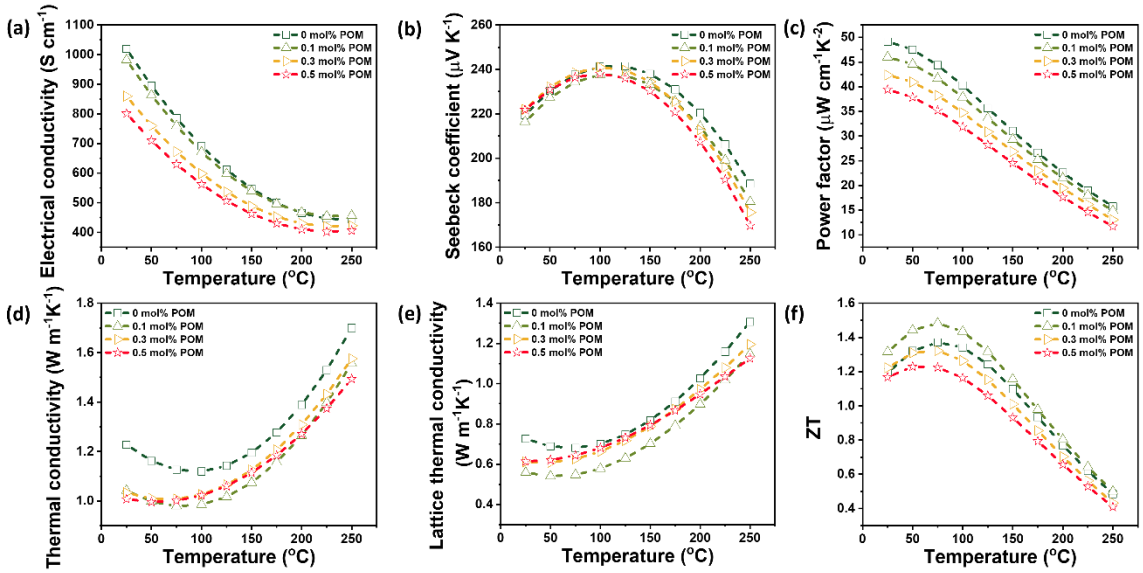

Fig. S13 Temperature-dependent TE properties of POM-coated BiSbTe; (a) electrical conductivity, (b) Seebeck coefficient, (c) power factor, (d) thermal conductivity, (e) lattice thermal conductivity, and (f) *ZT*.

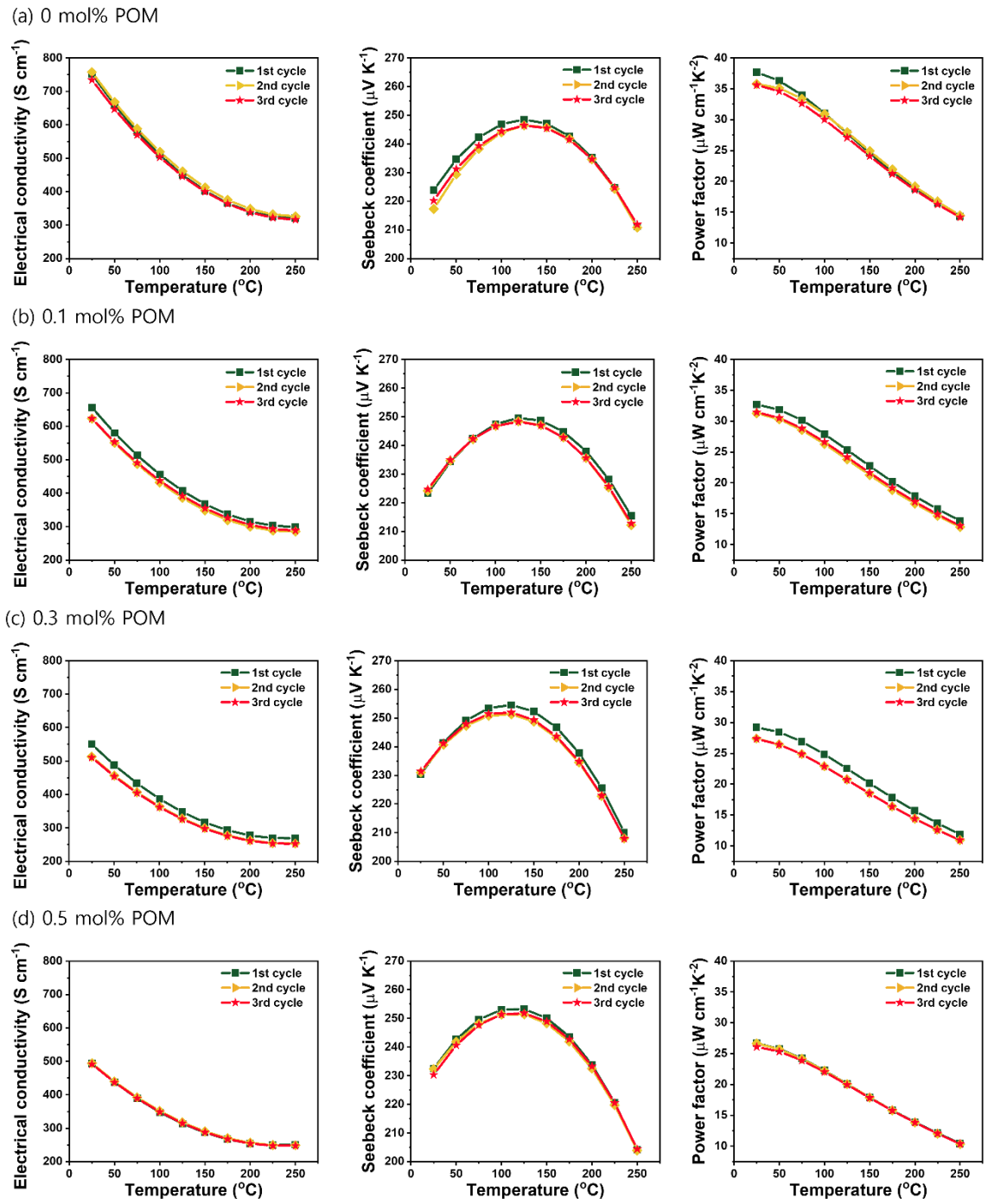

Fig. S14 Temperature-dependent electrical conductivity, Seebeck coefficient and power factor of (a)0 mol%, (b) 0.1 mol%, (c) 0.3 mol% and (d) 0.5 mol% POM-coated BiSbTe.

Table S1 Estimated effective masses of carriers of POM-coated BiSbTe as a function of the POM content.

	0 mol% POM	0.1 mol% POM	0.3 mol% POM	0.5 mol% POM
m^*/m_0	0.85	0.8	0.79	0.79

Table S2 Parameters for the calculation of lattice thermal conductivity.

Parameter	Description	Value	Method
v	Average speed of sound	2147 m·s^{-1}	S10
v_L	Longitudinal speed of sound	2884 m·s^{-1}	S10
v_T	Transverse speed of sound	1780 m·s^{-1}	S10
θ_a	Debye temperature	94 K	S10
V	Average atomic volume of $Bi_{0.5}Sb_{1.5}Te_3$	3.13×10^{-29} m^3	-
$V_{Bi_2Te_3}$	atomic volume of Bi_2Te_3	3.40×10^{-29} m^3	S10
$V_{Sb_2Te_3}$	atomic volume of Sb_2Te_3	3.13×10^{-29} m^3	S10
γ	Grüneisen parameter	2.3	S11
M	Average atomic mass of $Bi_{0.5}Sb_{1.5}Te_3$	2.22×10^{-25} kg	S10
$M_{Bi_2Te_3}$	Average atomic mass of Bi_2Te_3	2.79×10^{-25} kg	S10
$M_{Sb_2Te_3}$	Average atomic mass of Sb_2Te_3	2.07×10^{-25} kg	S10
Γ	Atomic size disorder scattering parameter	0.145	S10
r	Poisson's ratio	0.24	S10
d	Average grain size	1 μm	Experimental
N_D	Dislocation density	4.7×10^{10} cm^{-2}	Fitted
B_D	Magnitude of Burgers vector	1.27×10^{-9} m	Fitted
C_0	Concentration of Bi_2Te_3 in $Bi_{0.5}Sb_{1.5}Te_3$	0.25	-
K	Bulk modules	44.8 GPa	S10
R	Average radius of nano-precipitate	100 nm	Experimental
D_{matrix}	Mass density of matrix	6.5 g·cm^{-3}	Experimental
D_{np}	Mass density of nano-precipitate	6.47 g·cm^{-3}	-
V_{np}	Density of nano-precipitate	2.7×10^{14} cm^{-3}	Fitted

Table S3 The comparison of *ZT* values with the recent reports for BiSbTe

Material	Synthesis	ZT_{max}	Temperature [°C]	Ref.
0.1 mol% POM – $Bi_{0.47}Sb_{1.53}Te_3$	Melt-spinning	1.56	75	This work
V-doped $Bi_{0.5}Sb_{1.5}Te_{2.97}$	Melt-quenching	1.24	27	S12
0.4 vol% SiC-doped $Bi_{0.4}Sb_{1.6}Te_3$	Ball-milling	1.50	75	S13
3 mol% MXene - $Bi_{0.4}Sb_{1.6}Te_3$	Ball-milling	1.10	150	S14
$Bi_{0.5}Sb_{1.5}Te_3$	Zone-melting	1.29	77	S15
0.06 wt% Ag_9GaSe_6 - $Bi_{0.48}Sb_{1.516}Cu_{0.004}Te_3$	Melt-quenching	1.42	102	S16

Reference

S1. J. Callaway and H. C. von Baeyer, *Phys. Rev*., 1960, **120**, 1149.

S2. Y. K. Koh, Y. Cao, D. G. Cahill and D. Jena, *Adv. Funct. Mater.*, 2009, **19**, 610-615.

S3. H. S. Kim, S. D. Kang, Y. Tang, R. Hanus and G. J. Snyder, *Mater. Horiz.,* 2016, **3**, 234-240.

S4. W. Kim, S. L. Singer, A. Majumdar, J. M. Zide, D. Klenov, A. C. Gossard and S. Stemmer, *Nano lett*., 2008, **8**, 2097-2099.

S5. N. Mingo, D. Hauser, N. Kobayashi, M. Plissonnier and A. Shakouri, *Nano lett.,* 2009, **9**, 711-715.

S6. H. L. Zhuang, H. Hu, J. Pei, B. Su, J. W. Li, Y. Jiang, Z. Han and J. F. Li, *Energy Environ. Sci*., 2022, **15**, 2039-2048.

S7. J. He, S. N. Girard, M. G. Kanatzidis and V. P. Dravid, *Adv. Funct. Mater*., 2010, **20,** 764-772.

S8. W. Kim and A. Majumdar, *J. Appl. Phys*., 2006, **99**, 084306.

S9. K. H. Lee, H. S. Kim, W. H. Shin, S. Y. Kim, J. H. Lim, S. W. Kim and S. I. Kim, *Acta Mater*., 2020, **185**, 271-278.

S10. S. I. Kim, K. H. Lee, H. A. Mun, H. S. Kim, S. W. Hwang, J. W. Roh, D. J. Yang, W. H. Shin, X. S. Li and Y. H. Lee, *Science,* 2015, **348**, 109-114.

S11. X. Chen, H. Zhou, A. Kiswandhi, I. Miotkowski, Y. Chen, P. Sharma, A. Lima Sharma, M. Hekmaty, D. Smirnov and Z. Jiang, *Appl. Phys. Lett*., 2011, **99**, 261912.

S12. Y. Peng, X. She, H. Zhao, X. Luo, Q. An, G. Cai, Y. Liu, Y. Tang, and B. Feng, *J. Mater. Sci.: Mater. Electron.*, 2023, **34**, 1952.

S13. H. L. Zhuang, B. Cai, Y. Pan, B. Su, Y. Jiang, J. Pei, F. Liu, H. Hu, J.Yu, J. W. Li, Z. Wang, Z. Han, H. Li, C. wang and J. F. Li, *Natl. Sci. Rev.*, 2024, **11**, nwae329.

S14. V. C. S. Theja, V. Karthikeyan, D. S. Assi, H. Huang, V. Kannan, Y. Chen, C.-H. Shek, and V. A. L. Roy, *Adv. Mater. Technol*., 2024, **9**, 2301722.

S15. K. Fu, J. Yu, B. Wang, X. Nie, W. Zhu, P. Wei, W. Zhao and Q. Zhang, *J. Mater. Sci.: Mater. Electron*., 2024, **35**, 319.

S16. C. Zhou, J. Zhu, S. Zhang, Z. Zhang, Z. Zhang, J. Cai, Q. Zhang, R. Li, L. Fan, J. Xu, G. Liu, X. Tan, B. Liang, and J. Jiang, *Energy Environ. Sci.,* 2026, **19**, 1237-1249.